

In-material physical computing based on reconfigurable microwire arrays via halide-ion segregation

Received: 30 October 2024

Accepted: 22 May 2025

Published online: 01 July 2025



Dengji Li^{1,8}, Pengshan Xie^{1,8}, Yuekun Yang^{2,3}✉, Yunfan Wang¹, Changyong Lan⁴, Yiyang Wei⁴, Jiachi Liao¹, Bowen Li^{1,5}, Zenghui Wu¹, Quan Quan¹, Yuxuan Zhang¹, You Meng¹, Mingqi Ding¹, Yan Yan¹, Yi Shen¹, Weijun Wang¹, Sai-Wing Tsang¹, Shi-Jun Liang^{1,2}, Feng Miao^{1,2}✉ & Johnny C. Ho^{1,5,6,7}✉

Conventional computer systems based on the Von Neumann architecture rely on silicon transistors with binary states for information representation and processing. However, exploiting emerging materials' intrinsic physical properties and dynamic behaviors offers a promising pathway for developing next-generation brain-inspired neuromorphic hardware. Here, we introduce a stable and controllable photoelectricity-induced halide-ion segregation effect in epitaxially grown mixed-halide perovskite CsPbBr_{1.5}I_{1.5} microwire networks on mica, as confirmed by various in-situ measurements. The dynamic segregation and recovery processes show the reconfigurable, self-powered photo-response, enabling non-volatile light information storage and precise modulation of optoelectronic properties. Furthermore, our microwire array successfully addressed a typical graphical neural network problem and an image restoration task without external circuits, underscoring the potential of in-material dynamics to achieve highly parallel and energy-efficient physical computing in the post-Moore era.

Conventional computing hardware based on the Von Neumann architecture is increasingly challenged by latency, power consumption, and density issues. This architecture inherently limits information representation to binary states (0 or 1) and computing functionality to Boolean logic operations in silicon-based complementary metal-oxide-semiconductor (CMOS) transistors^{1,2}. In contrast, biological neural systems, which operate based on the dynamics of chemicals and ions, exhibit far superior energy efficiency and information processing capabilities. These systems function fundamentally differently from

CMOS transistors and circuits^{3–6}. Inspired by the structure and function of biological neural systems, there is growing interest in developing intelligent neuromorphic computing hardware that emulates the human brain. Such hardware aims to incorporate features like adaptation, threshold behavior, non-linearity, synaptic connectivity, and high parallelism. Examples include in-sensor retinomorph computing, in-memory neuromorphic computing, and physical neural networks implemented directly through physical processes within materials and devices^{7–16}. Exploring diverse intrinsic physical

¹Department of Materials Science and Engineering, City University of Hong Kong, Hong Kong SAR 999077, P. R. China. ²Institute of Brain-Inspired Intelligence, National Laboratory of Solid State Microstructures, School of Physics, Collaborative Innovation Center of Advanced Microstructures, Nanjing University, Nanjing 210093, P. R. China. ³School of Intelligence Science and Technology, Nanjing University, Suzhou 215163, P. R. China. ⁴State Key Laboratory of Electronic Thin Films and Integrated Devices, University of Electronic Science and Technology of China, Chengdu 610054, P. R. China. ⁵Shenzhen Research Institute, City University of Hong Kong, Shenzhen 518057, P. R. China. ⁶State Key Laboratory of Terahertz and Millimeter Waves, City University of Hong Kong, Hong Kong SAR 999077, P. R. China. ⁷Institute for Materials Chemistry and Engineering, Kyushu University, Fukuoka 816-8580, Japan. ⁸These authors contributed equally: Dengji Li, Pengshan Xie. ✉e-mail: yangyk@nju.edu.cn; miao@nju.edu.cn; johnnyho@cityu.edu.hk

dynamics, such as ion migration and segregation in emerging materials, is crucial for achieving innovative physical computing hardware with enhanced architecture, efficiency, and intelligence.

Photoelectricity-induced halide-ion segregation (PEHS) is typically detrimental in mixed-halide perovskite optoelectronic devices due to its negative impact on charge mobility and carrier lifetime, leading to halide-rich domains and localized bandgap variations^{17–19}. However, this PEHS phenomenon can be actively controlled and visualized using light and electrical bias. Characteristic photoluminescence peaks revert after removing external stimulation, illustrating ion migration from and back into the initially excited perovskite materials^{20,21}. More importantly, as the halide distribution changes, mixed-phase perovskites exhibit luminescence variations and generate non-volatile intrinsic electric fields. This results in a continuous self-powered bidirectional photocurrent phenomenon within the material^{22–24}. In addition, driven iodide ion drift has been reported to manipulate the photocurrent direction in trihalide perovskite photovoltaic devices using electric pulses. Consequently, a stable and controllable PEHS effect in mixed-halide perovskites holds promising potential for developing low-cost neuromorphic systems.

In this article, we unveil the discovery of a stable and controllable PEHS effect in epitaxially grown mixed-halide perovskite CsPbBr_{1.5}I_{1.5} microwire (MW) networks on mica. This innovative effect enables a switchable, self-powered photoresponse during halide phase segregation, facilitating non-volatile light information storage and pixel-level modulation of optoelectronic properties. By leveraging the growth morphologies of perovskite arrays and networks, we demonstrate neuromorphic architectures capable of parallel computing and image restoration. This approach seamlessly integrates machine vision with parallel computing, potentially reducing reliance on backend processing and significantly optimizing computational efficiency.

Results

Physical computing based on optoelectronic reconfigurable microwires

For the all-in-one sense-storage-computing chips, execution efficiency and power consumption are important issues that must be addressed. In order to achieve neural-like arithmetic functionality and to break the shackles of von Neumann architectures in the post-Moore era, energy-efficient all-in-one devices with neuron-like multifunctional architecture (parallel and random connectivity) demonstrate great development potential. Due to the ion migration characteristics in the PEHS effect and the continuously changing bandgap in mixed halide ratio perovskites, the two-terminal structure based on mixed-halide perovskite MW networks demonstrates a stable, reconfigurable, programmable, and self-powered photoresponse under multiple wavelength lasers. Moreover, the extent of the PEHS effect can be effectively tuned by both the external electric field and the illuminated power density, making it a promising candidate for machine recognition applications. As displayed in the central panel of Fig. 1a, there is no inner electric field in the initial uniformly mixed-halides perovskites. Hence, the measured I_{ds} – V_{ds} curve goes through the initial point. Under light and electrical stimulation, halide phase separation gradually occurs in the perovskite, generating internal electric fields closely related to the external stimulation field (left and right panel of Fig. 1a). After removing the external positive and negative voltage control, internal electric fields opposite the external fields are formed within the perovskite, which we define as the p - p^+ and p^+ - p states²⁵. Accordingly, with the formation of the internal electric field, the perovskite exhibits corresponding self-powered positive and negative photoconductivity.

Based on these unique electrical characteristics, mixed-halide perovskite devices are particularly well-suited for high-parallelism synchronous computation due to their flexible hardware configuration capabilities. However, to achieve dynamic resource allocation

and enable the simultaneous execution of multiple tasks or operations, maintaining stability in the configurable properties is crucial. Therefore, perovskite parallel arrays were selected to assess the operational stability and reliability of the PEHS effect during manipulation. Scanning photocurrent mapping (SPCM) clearly reveals a distinct photocurrent array of +550 pA and –180 pA, compared to the mica background, in the p - p^+ and p^+ - p state arrays (Fig. 1b). These pronounced photocurrent patterns correspond directly with the perovskite MWs connected to both electrodes (Supplementary Fig. S1), highlighting the device's exceptional stability and reconfigurability.

The reconfigurable nature of these arrays allows for the real-time adjustment and optimization of hardware resources, enabling the efficient execution of complex parallel tasks with minimal latency. Based on the growth morphology of mixed-halide perovskite materials, we designed two processor types: parallel and random arrays. Parallel arrays show high row uniformity, with adjacent devices exhibiting voltage-modulated photoelectric behaviors akin to addition and subtraction. On the other hand, random arrays enable large-scale integration, with each device displaying an independent, specific random topology. Figure 1c illustrates a schematic combining an MW array with photonic interactions, where the MW array is programmed to carry matrix information and enables efficient parallel computation through photonic signals. In this scenario, real-world features like color accuracy and grayscale are extracted, converted into electrical signals, and input into pre-programmed arrays. These arrays perform matrix functions, producing output signals refined into high-quality results. This technology efficiently handles large data processing, with parallel computing greatly boosting speed and efficiency. The high programmability and stability of the MW array ensure accurate, reliable computation. Combined with visual recognition or complex tasks, it significantly improves processing speed, making it ideal for real-time applications.

Epitaxy growth of mixed-halide perovskite MW networks

In this study, neuromorphic device units were fabricated by direct evaporation of gold electrodes onto single-crystalline mixed-halide MW networks on mica. These CsPbBr_{1.5}I_{1.5} MWs were grown using a vapor-phase route, forming triangular prism structures ~1 μm in height. (Methods and Supplementary Fig. S2)^{26,27}. We realize the direct observation of the epitaxy growth of perovskites on the mica through HRTEM. Our segregated halide perovskite FIB samples were formed and attributed to a one-minute 5 V/μm voltage and continuous 30 mW cm^{–2} light exposure stimulation. Figure 2a shows a direct connection between the mica lattice and perovskite lattice rather than the van der Waals gap, suggesting the direct epitaxy growth mechanism. Meanwhile, mixed-halide perovskite's [001] growth direction was parallel to [110] of the muscovite mica. I-based and Br-based perovskites were randomly distributed across the structure, with some amorphous regions due to halide diffusion (Fig. 2b). Domain boundaries, 2–3 nm wide, contained partial screw dislocations with the Burger's vector along the [100] direction (Fig. 2cii–iv, and Supplementary Fig. S3). These I-rich, Br-rich, and transition zones showed edge dislocations from stress during phase separation. Shear transformations induced similar dislocations near boundaries with minimal lattice misalignment. Diffraction analysis revealed dislocation patterns at the Br/I interface. Images of the mica substrate showed the 2M1 polytype structure of muscovite with a 19.9 Å interplanar spacing (Fig. 2d and Supplementary Fig. S4)^{28,29}. The (100) and (010) perovskite planes exhibited similar but slower growth rates compared to the (001) plane (Fig. 2e). A ~1.6% mismatch between the (110) plane of CsPbI₃ and the (001) plane of muscovite confirmed direct epitaxy (Fig. 2d, e). Energy-dispersive X-ray spectroscopy (EDS) mapping revealed a distinct interface between the halide perovskites and mica, with no significant diffusion (Fig. 2f and Br/I ratio in Supplementary Fig. S5). These

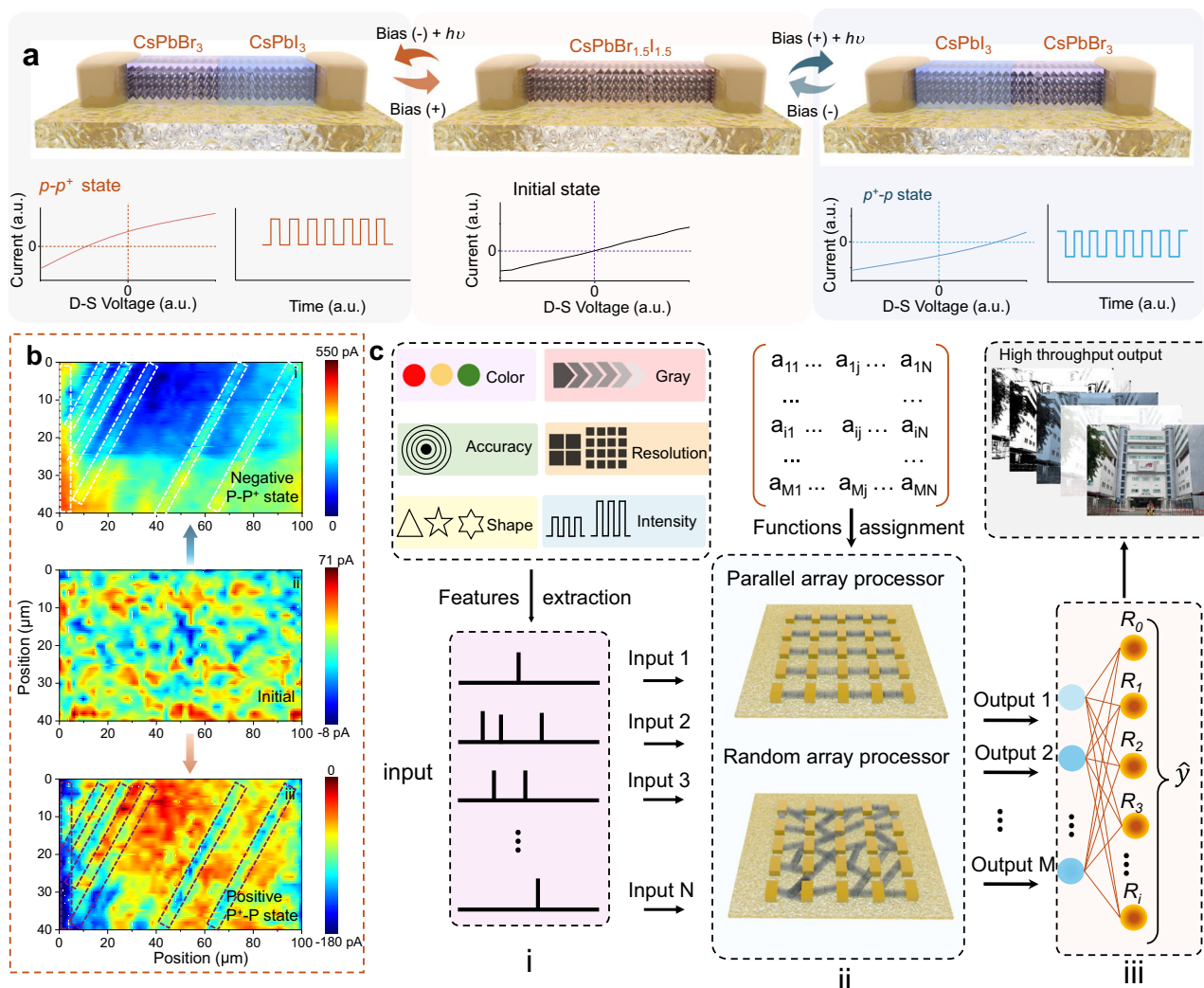


Fig. 1 | Schematic of reconfigurable performance, mechanism, and algorithm application. **a** Schematic diagrams of the PEHS effects on CsPbBr_{1.5}I_{1.5} MWs and the corresponding reconfigurable self-powered optoelectronic performance. **b** SPCM

of the parallel arrays of the modulated $p-p^*$, initial, and p^*-p states. **c** Schematic diagrams of the process of physical computing.

observations were further validated by X-ray diffraction and scanning electron microscopy (Supplementary Figs. S6 and S7).

While standard lattices suggest favorable vacancy-assisted halide ion diffusion, the precise migration mechanism under external stimuli remains unclear. Cs⁺ migration has an activation energy of 0.77 eV, likely a lower limit, as the ideal migration path hinders long-range transport^{30,31}. Pb²⁺ vacancy migration, with a much higher energy barrier of 2.31 eV, indicates a stable Pb sublattice^{32,33}. This supports the thermodynamic stability of the inorganic lead iodide sublattice in perovskites and suggests cation diffusion is likely the rate-limiting step in crystal growth^{34,35}. Instead of a linear jump, halide ions likely follow a curved path around Pb²⁺ ions (Fig. 2g for Br-migration, Fig. 2h for I-migration)^{36–38}. Calculations (see “Methods”) show I-migration has a lower energy barrier (0.586 eV) than Br-migration (1.356 eV), making I diffusion more efficient. This suggests that reverse bias can easily drive I ions or vacancies to drift, forming segregated I-rich or Br-rich regions and flipping the $p-i-p^+$ structure to a p^*-i-p configuration.

Switchable halide-ion segregation effect with light and bias

Here, those mixed-halide single-crystal MW networks were adopted to visualize the switchable PEHS effect away from grain boundaries. A confocal microscope (Fig. 3a) measured continuous

photoluminescence (PL) spectra from a fixed position in the MWs using 400-nm laser illumination at 20 mW cm⁻². Spectra were recorded every 0.1 sec, with time-dependent changes shown in Fig. 3b under different electrical biases. Initially, a stable emission peak appeared at ~591 nm with no bias. Applying a +30 V bias resulted in three peaks at 552.5 nm, 591 nm, and 695 nm (Supplementary Fig. S8a). Within ~2 sec, the main peak blue-shifted from 591 nm, creating a strong peak at 552.5 nm and a weak peak at 695 nm, while the 591 nm peak decayed nearly to zero, indicating the segregation of mixed-halide ions and the movement of iodine ions away from the excited region. When the external bias was switched to -30 V, the emission peak at 552.5 nm began to redshift, returning the phase-segregated condition to the initial mixed-halide state (Supplementary Fig. S8b). Finally, after removing the external bias, the emission peak stabilized at 591 nm. In this case, the initial blue shift driven by the positive bias indicates the formation of Br-rich domains and serves as a clear signature of PEHS^{39,40}. As the external bias increases, emission peaks from Br-rich, uniform I-Br, and intermediate halide states are observed. The decline of the peak at 591 nm and the growth of a wide-bandgap peak at 552.5 nm suggest that the uniform I-Br domains decompose, iodine ions are driven away, and the as-grown Br-rich composition forms at a high intensity (Supplementary Fig. S8a). Adjusting the external bias

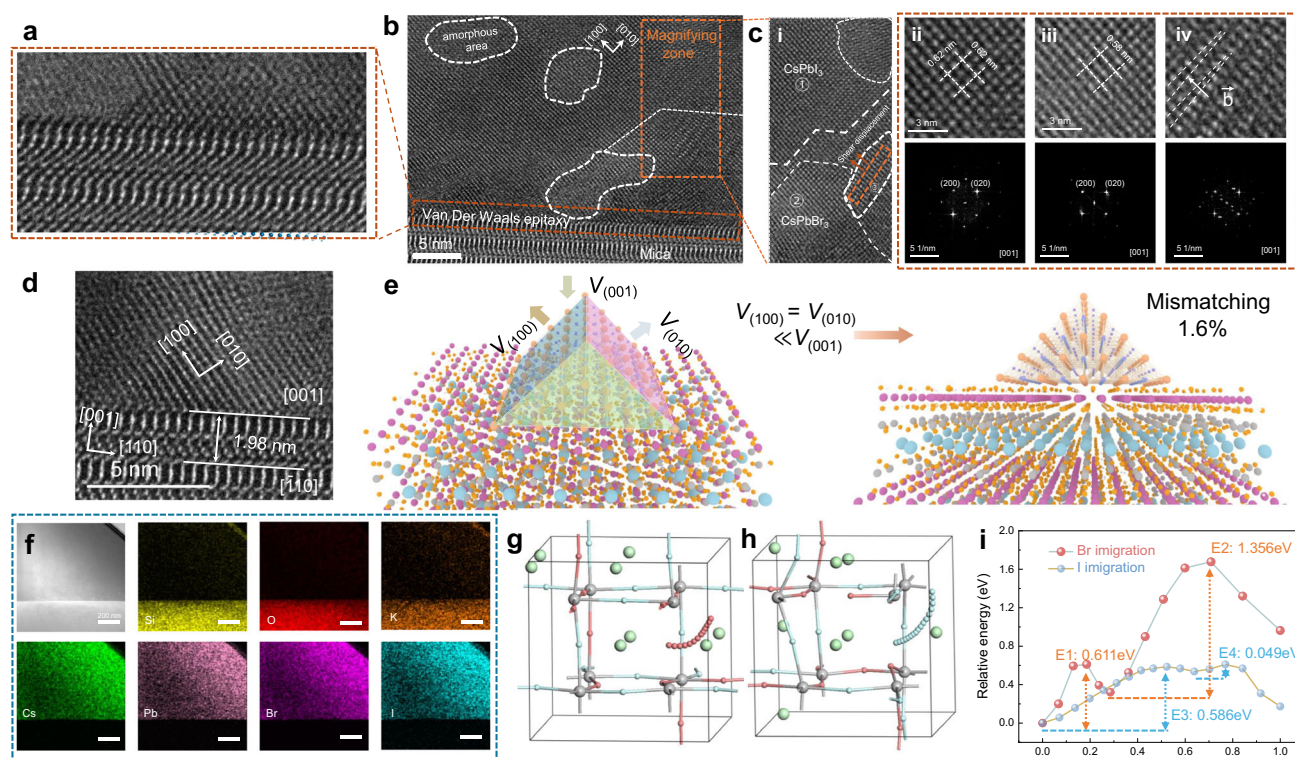


Fig. 2 | Material characteristics of the mixed-halide perovskite MWs. a–d The HRTEM images of the mixed-halide perovskite on mica. Inside, a and d display the epitaxy relation of perovskite and mica, while b and c show the interface of Br-rich and I-rich regions. **e** Schematic diagrams to show the epitaxy growth relationship of

CsPbX₃ on mica and the corresponding growth mechanism. **f** EDS mapping of the sample FIB slides. **g, h** The models of the migration path of Br (**g**) and I (**h**) ions. **i** Corresponding energy profile.

density (Supplementary Fig. S9) produces stable PL spectra, showing a strong link between halide ion distribution and bias power. This process is termed bias-modulated halide-ion separation (BMHS). Notably, after the external stimulus is removed, segregated halide ions gradually return to their original positions due to the concentration gradient⁴¹ or the mixing entropy^{40,42}. Applying reverse bias accelerates this mixing while removing the bias restores the initial distribution. This reversible behavior confirms that halide ion distribution is controlled by the external bias. In contrast, the emission wavelength of pure CsPbBr₃ remains unchanged under varying bias (Supplementary Fig. S10), indicating that the effect is unique to mixed-halide systems and not due to degradation or heating. No significant sample degradation was observed throughout the measurement.

Focusing on PL density, Fig. 3b and Supplementary Fig. S11a show a significant drop in overall intensity when applying a 30 V external bias. After removing the bias, the PL intensity recovered to about 40% of its initial value within 10 minutes (Supplementary Fig. S11b and S12). When the bias was reversed, the PL intensity quickly rebounded to around 80% in under one minute (Supplementary Fig. S13). As shown in Fig. 3c, this phenomenon is thought to be closely linked to the evolution of alloyed perovskite lattices from phase homogeneity to segregation and back under operational stressors like light and bias^{21,43}. A previously proposed model suggests that charge carriers may couple with the soft lattice to form polarons, creating enough strain to drive halide segregation and form iodine-rich domains^{44–47}. Existing explanations do not account for controllable phase segregation in CsPbBr_{1.5}I_{1.5} MW networks under high external bias. We propose a lattice model based on polaron-induced segregation to explain changes in halide distribution with varying biases. This model considers three stages of driving forces: 1) excitation and local aggregation of iodine towards polarons due to the external electric field (stages i to ii),

2) migration of iodine-rich regions under the inverse electric field (stage ii to iii), and 3) homogeneous mixing of halides when strong strain gradients are absent (stage iii to iv). Additionally, lattice distortion strongly correlates with the extent of Br-I phase separation, significantly impacting the material's emission and optoelectronic properties. The typical emission peak characteristics at different stages are shown in Fig. 3d. Within this framework, remixing occurs under reverse bias as strain gradients are reduced where polarons overlap or merge.

To validate the model, we used confocal fluorescence microscopy to observe emission behavior in our samples under different external biases. As shown in Fig. 3e, applying a positive bias caused significant fluorescence attenuation in both the green (500–570 nm) and red (640–700 nm) regions, while an inverse bias led to noticeable enhancement. Additional fluorescence images from continuous measurements are provided in Supplementary Figs. S14 and S15. These results align with the changes in PL density, supporting the proposed models. The model suggests that phase segregation responds rapidly to external bias, while natural recovery through halide ion diffusion is slower. Clear bandgap differences were observed between phases^{25,48}. Beyond the distinct emission effects, a local electric field is generated within the perovskite MWs due to bias-induced phase segregation, with its direction controlled by adjusting the I-rich region via external bias. Detailed self-powered photoresponse characteristics are discussed in the Supplementary materials.

Reconfigurable self-power photoresponse

To better understand the effect of composition tuning on the internal electric field, a simplified process is introduced, focusing only on the initial mixed states and fully segregated Br-I states (Supplementary Fig. S16a). The electric field mechanism in this system is driven by the

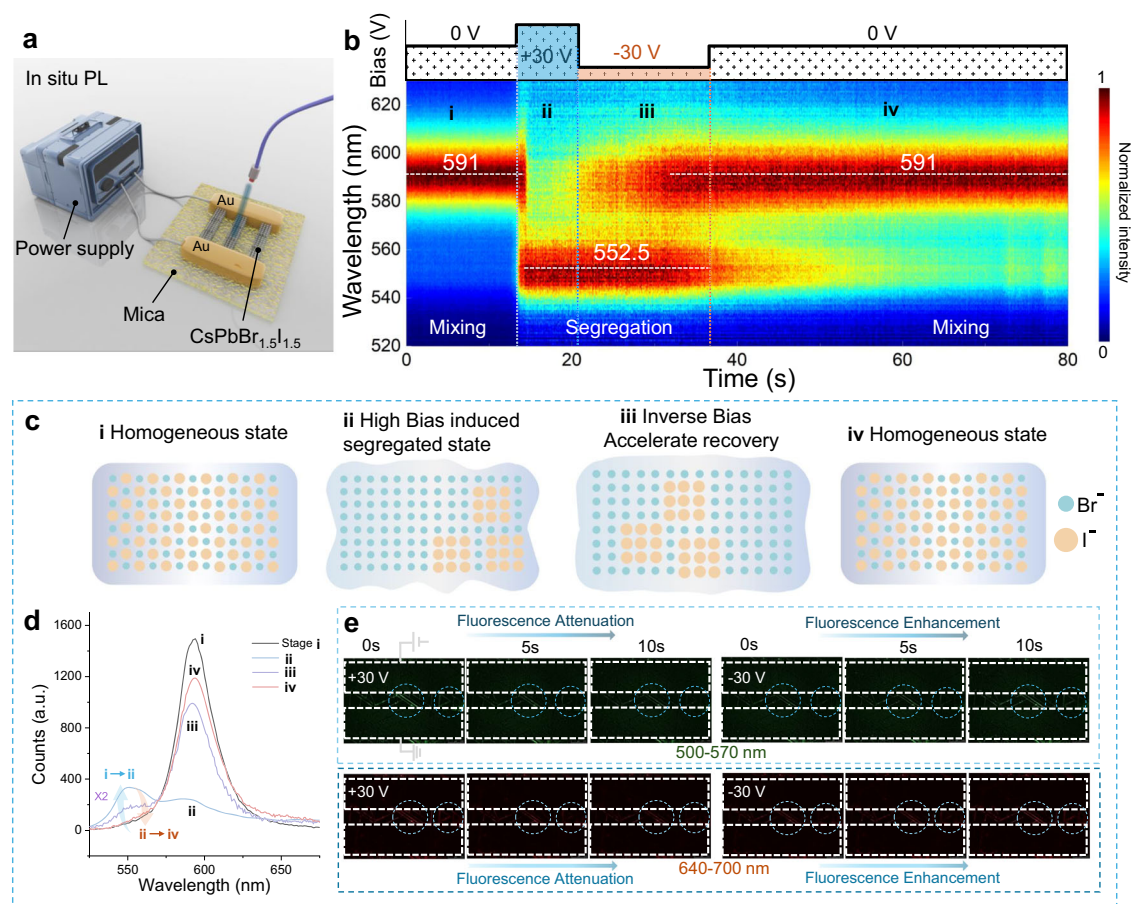


Fig. 3 | Photoelectricity-induced halide-ion segregation (PEHS) and mixing within CsPbBr_{1.5}I_{1.5} MWs. **a** Schematic of the confocal PL microspectroscopy system. **b** Normalized PL emission spectra recorded upon illumination of 20 mW cm⁻² with applied 0 V 20 s, followed by applied +30 V for 2 s, then inverse to

−30 V for 10 s, and eventually removing the bias. **c** Schematic diagram of 4 stages in the whole bias-modulated PEHS process. **d** PL spectra of the corresponding stages. **e** Fluorescence variables of the perovskite MWs in the bias-modulated process.

bandgap difference between CsPbBr₃ and CsPbI₃, with the field direction from the Br-rich region (*p* state) to the I-rich region (*p*+ state). This aids in clarifying the field dynamics^{25,48}. To assess the impact of composition tuning during halide-ion segregation, devices from PS emission studies were measured under similar conditions. The source-drain current (*I*_{ds}) versus source-drain voltage (*V*_{ds}) was recorded for devices under varying bias pulses, with and without light illumination (Supplementary Fig. S16b, c). Before applying external bias, the *I*_{ds}–*V*_{ds} curve passes through the origin, confirming good ohmic contact between the Au electrode and the initial mixed-state networks, as gold electrodes typically do not favor a particular charge transport direction. With varying bias pulses applied, the electric field inside the network was measured even in the dark, showing a directional photovoltaic effect for both positive and negative pulses. This highlights the influence of *V*_{ds} on the internal polarity of the mixed-halide perovskite photodiode. The device's self-powered photoresponse was then measured, with photocurrent (*I*_{ph} = *I*_{light} – *I*_{dark}) defined as the current difference between light and dark conditions per unit area. After a positive pulse, *I*_{ph} is negative. In contrast, a negative pulse makes it positive (Supplementary Fig. S16d). A tunable self-powered photoresponse was observed across the NUV to NIR range, producing consistent positive and negative photocurrents under 450 nm, 532 nm, and 1550 nm laser illumination (Supplementary Figs. S16e–g, S17–19).

Next, with a fixed bias pulse of 1 V/μm for 5 s applied under all laser wavelengths, the self-powered photoresponse at varying light

intensities was investigated. In deep learning, light intensity is treated as pixels in trained images, with the intensity-photocurrent relationship impacting the computational outcome. The photo-response (Supplementary Fig. S16e) was tested at different intensities (0.4–24 mW cm⁻² for 450 nm, 5 to 16.5 mW cm⁻² for 532 nm, and 70 to 840 mW cm⁻² for 1550 nm), showing a positive correlation between photocurrent and power density as higher photon flux generates more carriers. All data were compiled in Supplementary Fig. S16h–j and Supplementary Fig. S17–19, fitting the power law equation *I*_{ph} ∝ *P*^α. The α values from inverse positive bias manipulation were closer to 1 than from initial bias manipulation, indicating lower trap density due to lattice distortion during segregation, consistent with our models. For 1550 nm, the photon energy alone is not sufficient to excite Br-I perovskites, but the thermal effect of the laser influences the halide-ion segregation, enabling a photo-response. The devices showed sub-linear behavior under 450 and 532 nm and super-linear behavior under 1550 nm due to varying recombination probabilities of photogenerated or hot carriers caused by trap states during segregation. Moreover, the single-MW optoelectrical comparison characterization was conducted to elucidate the underlying physical mechanisms. Supplementary Fig. S20a indicates sub-ms response dynamics of the single-MW device. Meanwhile, Supplementary Fig. S20b displays the self-powered time-resolved photocurrent data for an individual MW under 0.1–5 mW cm⁻² 450 nm illumination. Besides, the regulatory performance of devices with multiple micron wires strongly

correlates with the number and dimensions of the micron wires between the channels (Supplementary Fig. S21).

Previous studies show that the power-dependent optoelectronic characteristics of the device are closely linked to the trap state density of the channel materials⁴⁹. With a continuous $\pm 0.5\text{ V}/\mu\text{m}$ bias (Supplementary Fig. S22), the photocurrent gradually saturated as power density increased, indicating more photogenerated carriers were trapped due to increasing trap density or an enhanced inverse inner electric field during halide-ion segregation. To confirm that the reconfigurable bias-manipulated photovoltaic effect is independent of electrodes, a comparison with Au-Ni electrodes was made. Since Au and Ni have similar work functions, minimizing Schottky barrier effects, the Au-Ni device showed similar photoconductive responses (Supplementary Fig. S23), confirming that the electrical performance is not influenced by electrode effects or contact interfaces.

The photocurrents (Supplementary Fig. S24) displayed varied hysteresis loops depending on the scanning direction, with a positive inner bias for the -1 V -to- 1 V scan and a negative bias for the reverse scan, consistent with the proposed model. For Au electrodes, V_{oc} ranged from 0.5 V to -0.6 V , while for Ni electrodes, it ranged from 1 V to -1 V , reflecting differences in charge carrier storage and transport. Here, V_{oc} was defined as the open-circuit voltage measured under illumination at zero current flow. With better chemical stability and conductivity, Au electrodes provided more stable operation under photoelectric stimulation. As shown in Supplementary Fig. S25, the device capacitance increased consistently as the bias decreased, peaking at zero bias. The exponential decrease in capacitance under reverse bias aligns with P-N junction barrier capacitance trends, while the symmetric behavior reflects the reconfigurable nature of the P-N junction⁵⁰. This symmetry supports the PEHS model and its link to reconfigurable photovoltaic effects, confirming its validity and potential for neuromorphic computing applications.

Next-generation computing hardware requires 1) a high density of configurable computing units for parallel operations; 2) a high-speed, high-bandwidth interconnect network with low power consumption; and 3) simple preparation and integration methods. To address these requirements, the precise response time was obtained under standardized operational conditions (450 nm illumination at $12\text{ mW}/\text{cm}^2$), which aligns with prior findings (Supplementary Fig. S26a). Additionally, endurance testing was performed under 11 repeated modulation cycles at $-0.4\text{ V}/\mu\text{m}$ to evaluate the device's durability. The results (Supplementary Fig. S26c) reveal that the device maintained relatively stable self-powered performance across these 11 cycles, with no notable decline in overall performance. Subsequently, we have enriched the work with ambient stability test data collected over 1000 sec under controlled conditions (25°C , $40\text{--}50\%$ relative humidity). These findings (Supplementary Fig. S26b and S26d) underscore the halide perovskite device's reliable operational stability over extended durations, with no significant deterioration in performance metrics. While our proposed approach makes progress toward achieving a high-density, low-power parallel system, there are still areas that require further development. Continued efforts and advancements will be necessary to address these challenges fully.

Besides, we tested the communication effect between two devices during bias manipulation. The SEM images and schematic (Supplementary Fig. S27) show that the connected devices demonstrated the desired self-powered configurable performance. Applying varying bias to one device controlled the entire system's performance, switching from -1.75 nA to 0.75 nA photocurrent, indicating a series-combined mechanism.

Implementation of physical computing by two kinds of microwire arrays

The traveling salesperson problem (TSP) (Fig. 4a) involves finding the shortest path to visit a set of cities and return to the starting point, with

applications in logistics, chip manufacturing, and route planning. Due to its computational complexity and finding a global optimal solution, solving TSP is difficult with conventional hardware. However, the polymorphic MWs van der Waals array allows for integrating highly parallel arrays for efficient problem-solving. We propose a 5×5 parallel array (Fig. 4b) to demonstrate solving a TSP involving four cities. Optoelectronic stimuli encode the node parameters (distances), enabling optimal solutions through matrix operations. Each device in these arrays shows analog-modulated performance (Supplementary Fig. S28), with overall performance being the cumulative output of each pixel device. As illustrated in the flow chart in Fig. 4biii, the final histogram accurately identifies the lowest photocurrent for tasks 2 and 4, confirming the effectiveness of the parallel array in high-parallelism computing. Furthermore, when integrated with edge enhancement algorithms, this reconfigurable, non-volatile bidirectional photoconductor significantly enhances image perception details while optimizing hardware and software power consumption. Specifically, edge enhancement for the “CityU” and “Nanjing University” logos was achieved by mitigating the contrast difference between the logo patterns (black) and the background (white). As illustrated in Supplementary Fig. S29, the device effectively reproduces the image features demonstrated in the simulation results, showcasing its capability to replicate intricate details accurately.

Deep learning with convolutional neural networks (CNNs) is crucial for image recognition in machine vision, but image contrast significantly affects accuracy. In image restoration, one challenge is information loss due to low contrast. For a different morphology of MW arrays, a random large-area distribution can achieve pixel-level image modulation. Moreover, for grayscale images with complex and diverse pixel gradient directions, the random topological properties demonstrate unique advantages in both restoration/repair and processing/recognition tasks. We used a 3×3 random array to simulate repairing damaged images. Each of the nine devices generated non-volatile positive and negative photoconductivity by being programmed with photoelectric signals, enhancing overall image contrast. By adjusting the grayscale range, we can regulate image contrast; a broader grayscale range results in higher contrast and more detail (Fig. 4f). To simulate contrast degradation from occlusion or damage, we first input an “H”-shaped signal into the array (Fig. 4d). The “H” sections generate positive current signals. In contrast, the other sections produce negative signals. The occluded region is defined as the two lower left areas where the light signal is reduced to one-tenth of the initial level. Despite significant damage to the “H”-shaped light signal, the displayed shape is still noticeably restored, and this restoration effect remains stable for 120 sec without significant degradation (Supplementary Fig. S30).

Based on actual device test results, we assigned values to the restored effects according to the image's grayscale range. As shown in Fig. 4g, we evaluated the performance of a standard three-layer CNN under different contrast conditions. Details of CNN's deep learning process are in the “Methods” section. In Fig. 4h, the network demonstrates strong robustness, maintaining high accuracy at 94.5% within the normal grayscale range. However, as the range narrows (indicating reduced contrast), accuracy declines and sharply drops. This decline occurs because the neural network struggles to distinguish edge details and capture key features in low-contrast images. Supplementary Fig. S31 shows confusion matrices reflecting a similar trend to the accuracy curve under standard and reduced contrast conditions. Given the significant impact of image distortion on visual recognition, we also assessed how different grayscale ranges affect recognition accuracy when the object is distorted. In Fig. 4i, we verify whether the recognition capabilities of original and distorted images follow similar patterns under varying contrast conditions. After reducing the grayscale range, the inset illustrates the contrast changes in the original and distorted MNIST images, highlighting the need for machine

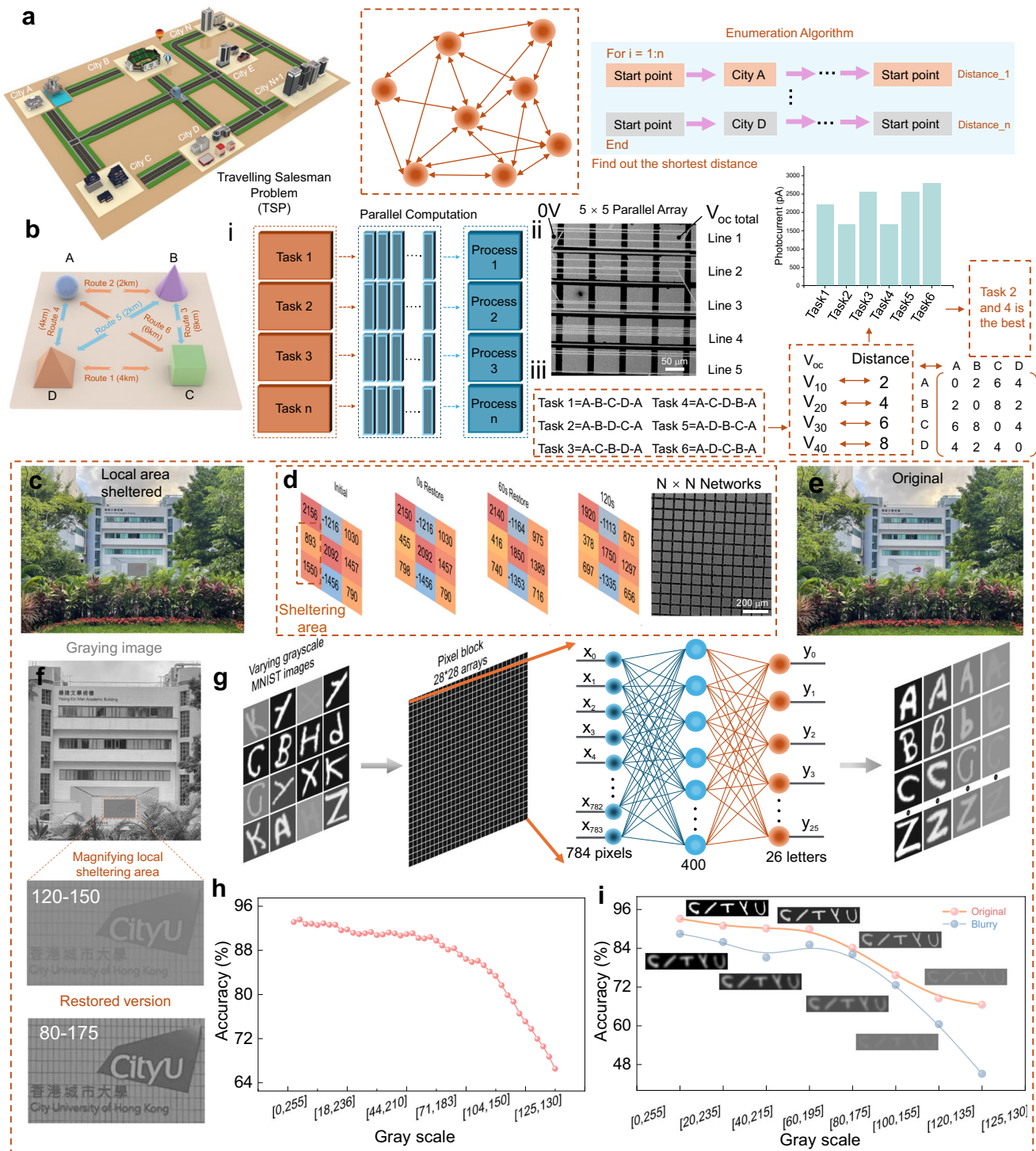


Fig. 4 | High parallelism computing and machine vision. a, b Illustration of the TSP and corresponding high parallelism computing process. **c, e** The photograph of CITYU's symbolic building with and without local area sheltered. **d** The actual testing performance and corresponding device to mimic the image restoration. **f** Grayscale conversion of the color photo and the effects corresponding to

different grayscale ranges. **g** Schematic diagram of the machine vision based on a convolutional neural network for letter image recognition. **h** The image recognition rate as a function of the grayscale. **i** Recognition rate of machine vision as a function of gray scale for normal and blurry images. The inset shows the results of the visual adaptation simulation for the MNIST image "CITYU".

recognition systems to capture and analyze image features based on contrast efficiently. Additional grayscale letter images are provided in Supplementary Fig. S32.

In conclusion, this work demonstrates the potential of PEHS in epitaxially grown mixed-halide perovskite MW networks as a promising route for next-generation neuromorphic hardware. The stable and

controllable PEHS effect, verified by in-situ photoluminescence measurements, enables non-volatile light information storage and precise modulation of optoelectronic properties. The dynamic segregation and recovery processes and the reconfigurable self-powered photo-response highlight the material's capability for physical computing. Successfully solving the classic TSP and an image restoration task

without external circuits emphasizes the significant potential of leveraging material-intrinsic dynamics to achieve highly parallel and energy-efficient computation. These findings offer valuable insights into developing brain-inspired hardware for advanced computing applications in the post-Moore era.

Methods

Preparation of CsPbBr_{1.5}I_{1.5} MW arrays and networks

The primary materials, PbI₂ (99%) and CsBr (99.999%) powders, were sourced from Sigma-Aldrich without additional purification. Initially, 100 mg of PbI₂ and 70 mg of CsBr were finely ground in an agate mortar for approximately ten minutes, producing a pale yellow powder. This mixture was then pre-annealed at 340 °C for 10 minutes, transforming into a reddish-brown powder. The mica substrate was then mechanically exfoliated to obtain a clean, uniform two-dimensional surface and positioned at the downstream end of a two-zone CVD system. The reddish-brown precursor powder was placed at the center of the first heating zone, about 15 cm from the mica. The system was subsequently evacuated to around 7 mTorr, and 300 sccm of high-purity argon gas (Ar, 99.999%) was introduced to purge the tube furnace. The argon flow rate was then adjusted to 70 sccm, and the pressure for growth was stabilized at 0.85 Torr. The first heating zone was gradually raised to 440 °C over 50 minutes and maintained at this temperature for another 60 minutes, while the second heating zone was kept steady at 310 °C. Finally, a reddish-brown product was deposited on the mica as the furnace cooled to room temperature in an argon atmosphere. Using this method, we can obtain a parallel array of mixed-phase perovskites. Moving the mica substrate in the second heating zone 5 cm closer is required to achieve a randomly networked sample, reducing the distance from the precursor to about 10 cm and lowering the growth pressure to 0.6 Torr. This adjustment will result in a randomly networked mixed-halide perovskite structure.

Material characterization

Our sample slices were prepared using an American-made FEI Helios 5 Hydra CX for focused ion beam (FIB) milling. The corresponding observations were obtained using high-resolution transmission electron microscopy (HRTEM) images and energy-dispersive X-ray spectroscopy (EDS) mapping from an American-made FEI Talos F200x. The crystalline phases of the samples were characterized using an X-ray diffraction (XRD) system (D2 Phaser with Cu K α radiation, Bruker). The surface morphology was examined with an optical and scanning electron microscope (Quanta 450 FEG, FEI). Elemental composition was confirmed through an energy-dispersive X-ray (EDX) detector attached to the Quanta 450 FEG. The continuous fluorescence characterization of the material was observed and recorded using a Laser Confocal Scanning Microscope (Leica SPE), with an external control voltage supplied by a source meter (KEYSIGHT B2912). The steady-state photoluminescence (PL) spectra were recorded using an F-4600 fluorescence spectrophotometer (HITACHI), while time-resolved PL data were obtained from a HORIBA Fluoromax-4. In-situ PL spectra under varying conditions were measured with a custom-built system utilizing a spectral CCD array spectrometer (Ocean Optics USB2000).

Preparation and characterization of the device

All the optoelectronic devices here were fabricated using an evaporation method with custom-designed patterns. The gold electrodes were deposited by thermal evaporation, while the nickel electrodes were created using electron-beam evaporation. To enable external voltage control during real-time monitoring of the material's photoluminescence changes and fluorescence effects, we designed mask patterns with 5 mm and 1 mm channel lengths. We used mask patterns with a channel length of 20 μ m for device designs aimed at algorithm verification. All electrodes were deposited to a thickness of 50 nm. The optoelectronic properties of all devices were measured using a

standard electrical probe station equipped with a semiconductor analyzer (Agilent 4155 C). A homemade light chopper was employed to control the light for the 405, 450, 532, and 635 nm lasers, while an attenuator was used to adjust its intensity. In contrast, the 1550 nm laser utilized an attached modulator (AFG 2005, Arbitrary Function Generator, Good Will Instrument Co. Ltd) to modulate the infrared (IR) irradiation. Illumination laser power was measured using a PM400 power meter (Thorlabs).

SPCM measurement

To explore the operational stability and underlying working mechanism of the reconfigurable self-powered mixed-halide perovskite arrays based on PEHS, photocurrent mapping was performed using an integrated optoelectronic scanning system (ScanPro Advance, Metatest). The spot size was set to 2 μ m to achieve high spatial resolution. Before scanning, the device was subjected to varying bias voltages under 450 nm laser illumination at 12 mW/cm² to manipulate the PEHS effect. The applied voltage was controlled by a source/measure unit (2636B, Keithley).

DFT calculation method

All the computations related to the halide energy barrier were carried out using CASTEP's first-principles calculation framework. The exchange-correlation potential was approximated using the generalized gradient approximation (GGA) with the Perdew-Burke-Ernzerhof (PBE) formula and DFT-D correction^{51,52}. Spin-polarized calculations were performed, and the Broyden-Fletcher-Goldfarb-Shanno (BFGS) method was utilized to locate the ground state of the supercells. Convergence criteria were set to an energy change below 10⁻⁵ eV per atom, a force less than 0.02 eV/Å, stress under 0.05 GPa, and displacement change of less than 0.001 Å. The atomic wave functions were truncated at a cutoff energy of 450 eV. The diffusion energy barrier was identified as the highest point on the minimum energy path, determined using the linear/quadratic synchronous transit (LST/QST) method.

Deep learning

Based on the actual device test results, we assign values to the restored effects according to the grayscale range in the image. The specific steps are shown in Supplementary Fig. S33. A standard three-layer convolutional neural network (CNN) under different contrast conditions was conducted by training it 30 times using 110,000 MNIST images containing 26 letters, each with varying levels of graying. During training, the degree of graying was explicitly included as an additional parameter. The training data converged after 50 epochs. During the training of the CNN, the input consists of the grayscale information from 784 pixels of MNIST images. This data is first processed using MobileNetV2, which extracts and integrates pixel-specific features. The CNN then applies multiple convolutional layer filters to detect local features such as edges, textures, and patterns. These filters slide across the image, computing a weighted sum of pixel values to produce feature maps. Following this, the network creates hidden layers from the pixel information. The network is trained to categorize images and identify underlying patterns effectively. After several convolutional and pooling layers, the feature maps are flattened into a one-dimensional vector. This vector is passed through fully connected layers, which combine features to make final predictions. The output layer uses the SoftMax function to assign probabilities to different classes, allowing the network to classify the image into predefined categories.

Data availability

Relevant data that support the key findings of this study are available within the article and the Supplementary Information file. All raw data generated during the current study are available from the

corresponding author upon request. Source data are provided with this paper.

Code availability

The code is available at: <https://github.com/Eddy-Ho/DJ-Li.git>.

References

- Migliato Marega, G. et al. Logic-in-memory based on an atomically thin semiconductor. *Nature* **587**, 72–77 (2020).
- Xia, Q. & Yang, J. J. Memristive crossbar arrays for brain-inspired computing. *Nat. Mater.* **18**, 309–323 (2019).
- Milano, G. et al. In material reservoir computing with a fully memristive architecture based on self-organizing nanowire networks. *Nat. Mater.* **21**, 195–202 (2022).
- Wang, D. et al. Ultrafast silicon photonic reservoir computing engine delivering over 200 TOPS. *Nat. Commun.* **15**, 10841 (2024).
- Wang, Z. et al. Resistive switching materials for information processing. *Nat. Rev. Mater.* **5**, 173–195 (2020).
- Wang, Z. et al. Memristors with diffusive dynamics as synaptic emulators for neuromorphic computing. *Nat. Mater.* **16**, 101–108 (2017).
- Hezaveh, Y. D., Levasseur, L. P. & Marshall, P. J. Fast automated analysis of strong gravitational lenses with convolutional neural networks. *Nature* **548**, 555–557 (2017).
- Hill, M. Q. et al. Deep convolutional neural networks in the face of caricature. *Nat. Mach. Intell.* **1**, 522–529 (2019).
- Chai, Y. et al. In-sensor computing for machine vision. *Nature* **579**, 32–33 (2020).
- Li, X. et al. Power-efficient neural network with artificial dendrites. *Nat. Nanotechnol.* **15**, 776–782 (2020).
- Mennel, L. et al. Ultrafast machine vision with 2D material neural network image sensors. *Nature* **579**, 62–66 (2020).
- Kasai, H., Ziv, N. E., Okazaki, H., Yagishita, S. & Toyozumi, T. Spine dynamics in the brain, mental disorders and artificial neural networks. *Nat. Rev. Neurosci.* **22**, 407–422 (2021).
- Kar, K., Kornblith, S. & Fedorenko, E. Interpretability of artificial neural network models in artificial intelligence versus neuroscience. *Nat. Mach. Intell.* **4**, 1065–1067 (2022).
- Zhou, Y. et al. Computational event-driven vision sensors for in-sensor spiking neural networks. *Nat. Electron.* **6**, 870–878 (2023).
- Li, L. et al. Adaptive machine vision with microsecond-level accurate perception beyond human retina. *Nat. Commun.* **15**, 6261 (2024).
- Yang, Y. et al. In-sensor dynamic computing for intelligent machine vision. *Nat. Electron.* **7**, 225–233 (2024).
- Zhu, H. et al. Long-term operating stability in perovskite photovoltaics. *Nat. Rev. Mater.* **8**, 569–586 (2023).
- Motti, S. G. et al. Phase segregation in mixed-halide perovskites affects charge-carrier dynamics while preserving mobility. *Nat. Commun.* **12**, 6955 (2021).
- Zhao, Y. et al. Strain-activated light-induced halide segregation in mixed-halide perovskite solids. *Nat. Commun.* **11**, 6328 (2020).
- Zhang, H. et al. Phase segregation due to ion migration in all-inorganic mixed-halide perovskite nanocrystals. *Nat. Commun.* **10**, 1088 (2019).
- Mao, W. et al. Light-induced reversal of ion segregation in mixed-halide perovskites. *Nat. Mater.* **20**, 55–61 (2021).
- Xiao, Z. et al. Giant switchable photovoltaic effect in organometal trihalide perovskite devices. *Nat. Mater.* **14**, 193–198 (2015).
- Huang, K. et al. Manipulating the migration of iodine ions via reverse-biasing for boosting photovoltaic performance of perovskite solar cells. *Adv. Sci.* **9**, 2204163 (2022).
- Feng, S. et al. Complete suppression of phase segregation in mixed-halide perovskite nanocrystals under periodic heating. *Adv. Mater.* **36**, 2308032 (2024).
- Zhao, Q. et al. High efficiency perovskite quantum dot solar cells with charge separating heterostructure. *Nat. Commun.* **10**, 2842 (2019).
- Chen, J. et al. Vapor-phase epitaxial growth of aligned nanowire networks of cesium lead halide perovskites (CsPbX₃, X = Cl, Br, I). *Nano. Lett.* **17**, 460–466 (2017).
- Li, D. et al. Selective surface engineering of perovskite microwire arrays. *Adv. Funct. Mater.* **33**, 2302866 (2023).
- Kogure, T. Imaging of dioctahedral 2: 1 layers by high-resolution transmission electron microscopy (HRTEM): Possibility of recording the dehydroxylate. *Am. Mineral.* **92**, 1368–1373 (2007).
- Noe, D. C. & Veblen, D. R. HRTEM analysis of dislocation cores and stacking faults in naturally deformed biotite crystals. *Am. Mineral.* **84**, 1925–1931 (1999).
- Guo, L. et al. Two-terminal perovskite optoelectronic synapse for rapid trained neuromorphic computation with high accuracy. *Adv. Mater.* **36**, 2402253 (2024).
- Meggiolaro, D., Mosconi, E. & De Angelis, F. Formation of surface defects dominates ion migration in lead-halide perovskites. *ACS. Energy Lett.* **4**, 779–785 (2019).
- McGovern, L. et al. Reduced barrier for ion migration in mixed-halide perovskites. *ACS. Appl. Energy Mater.* **4**, 13431–13437 (2021).
- McGovern, L., Koschany, I., Grimaldi, G., Muscarella, L. A. & Ehrler, B. Grain size influences activation energy and migration pathways in MAPbBr₃ perovskite solar cells. *J. Phys. Chem. Lett.* **12**, 2423–2428 (2021).
- Leguy, A. M. et al. The dynamics of methylammonium ions in hybrid organic–inorganic perovskite solar cells. *Nat. Commun.* **6**, 7124 (2015).
- Weller, M. T., Weber, O. J., Henry, P. F., Di Pumpo, A. M. & Hansen, T. C. Complete structure and cation orientation in the perovskite photovoltaic methylammonium lead iodide between 100 and 352 K. *Chem. Commun.* **51**, 4180–4183 (2015).
- Eames, C. et al. Ionic transport in hybrid lead iodide perovskite solar cells. *Nat. Commun.* **6**, 7497 (2015).
- Islam, M. S. Ionic transport in ABO₃ perovskite oxides: a computer modelling tour. *J. Mater. Chem.* **10**, 1027–1038 (2000).
- Chroneos, A., Yildiz, B., Tarancón, A., Parfitt, D. & Kilner, J. A. Oxygen diffusion in solid oxide fuel cell cathode and electrolyte materials: mechanistic insights from atomistic simulations. *Energy Environ. Sci.* **4**, 2774–2789 (2011).
- Mao, W. et al. Visualizing phase segregation in mixed-halide perovskite single crystals. *Angew. Chem. Int. Ed.* **58**, 2893–2898 (2019).
- Barker, A. J. et al. Defect-assisted photoinduced halide segregation in mixed-halide perovskite thin films. *ACS. Energy Lett.* **2**, 1416–1424 (2017).
- DeQuilettes, D. W. et al. Photo-induced halide redistribution in organic–inorganic perovskite films. *Nat. Commun.* **7**, 11683 (2016).
- Tang, X. et al. Local observation of phase segregation in mixed-halide perovskite. *Nano. Lett.* **18**, 2172–2178 (2018).
- Huang, T. et al. Performance-limiting formation dynamics in mixed-halide perovskites. *Sci. Adv.* **7**, eabj1799 (2021).
- Bischak, C. G. et al. Origin of reversible photoinduced phase separation in hybrid perovskites. *Nano. Lett.* **17**, 1028–1033 (2017).
- Draguta, S. et al. Rationalizing the light-induced phase separation of mixed halide organic–inorganic perovskites. *Nat. Commun.* **8**, 200 (2017).
- Nie, W. et al. Light-activated photocurrent degradation and self-healing in perovskite solar cells. *Nat. Commun.* **7**, 11574 (2016).
- Hoffman, J. B., Schleper, A. L. & Kamat, P. V. Transformation of sintered CsPbBr₃ nanocrystals to cubic CsPbI₃ and gradient CsPbBr_xI_{3-x} through halide exchange. *J. Am. Chem. Soc.* **138**, 8603–8611 (2016).
- Tao, S. et al. Absolute energy level positions in tin- and lead-based halide perovskites. *Nat. Commun.* **10**, 2560 (2019).

49. Lopez-Sanchez, O., Lembke, D., Kayci, M., Radenovic, A. & Kis, A. Ultrasensitive photodetectors based on monolayer MoS₂. *Nat. Nanotechnol.* **8**, 497–501 (2013).
50. Wang, C. A., Fu, S., Liu, L., Li, J. & Bao, J. Temperature-dependent power-law analysis of capacitance-voltage for GaN-based pn junction. *J. Appl. Phys.* **123**, 134502 (2018).
51. Perdew, J. P. et al. Restoring the density-gradient expansion for exchange in solids and surfaces. *Phys. Rev. Lett.* **100**, 136406 (2008).
52. Perdew, J. P., Burke, K. & Ernzerhof, M. Generalized gradient approximation made simple. *Phys. Rev. Lett.* **77**, 3865 (1996).

Acknowledgements

D. Li and P.S. Xie contributed equally to this research, which was financially supported by a fellowship award from the Research Grants Council of the Hong Kong Special Administrative Region, China (CityU RFS2021-1S04), the Innovation and Technology Fund (MHP/O44/23) from the Innovation Technology Commission of the Hong Kong Special Administrative Region, China, the National Natural Science Foundation of China (62122036, 62034004, 62304104), the Science Technology and Innovation Committee of Shenzhen Municipality (Project No. JCYJ20230807114910021, JCYJ2023080711619039), and Guangdong Basic and Applied Basic Research Fund (Project No. 2024A1515011922, 2023A1515011752).

Author contributions

D.L. and P.X. contributed equally to this work. D.L., P.X., and J.C.H. designed and structured the experiments. D.L. and P. X. synthesized and characterized the microwires and devices. Y.Y., S.L., and F.M. carried out device simulations, while Y.W., C.L., Y.W., J.L., B.L., and Z.W. assisted with photoelectric performance measurements. Q.Q., Y.Z., Y.M., M.D., Y.Y., Y.S., W.W., and S.T. contributed to the data analysis. D.L., P.X., Y.Y., and J.C.H. co-wrote the paper. All authors discussed the results and provided feedback on the manuscript.

Competing interests

The authors declare no competing interests.

Additional information

Supplementary information The online version contains supplementary material available at <https://doi.org/10.1038/s41467-025-60530-w>.

Correspondence and requests for materials should be addressed to Yuekun Yang, Feng Miao or Johnny C. Ho.

Peer review information *Nature Communications* thanks Ji Hyun Baek, Abhishek Misra, and the other, anonymous, reviewer(s) for their contribution to the peer review of this work. A peer review file is available.

Reprints and permissions information is available at <http://www.nature.com/reprints>

Publisher's note Springer Nature remains neutral with regard to jurisdictional claims in published maps and institutional affiliations.

Open Access This article is licensed under a Creative Commons Attribution-NonCommercial-NoDerivatives 4.0 International License, which permits any non-commercial use, sharing, distribution and reproduction in any medium or format, as long as you give appropriate credit to the original author(s) and the source, provide a link to the Creative Commons licence, and indicate if you modified the licensed material. You do not have permission under this licence to share adapted material derived from this article or parts of it. The images or other third party material in this article are included in the article's Creative Commons licence, unless indicated otherwise in a credit line to the material. If material is not included in the article's Creative Commons licence and your intended use is not permitted by statutory regulation or exceeds the permitted use, you will need to obtain permission directly from the copyright holder. To view a copy of this licence, visit <http://creativecommons.org/licenses/by-nc-nd/4.0/>.

© The Author(s) 2025